



# In vitro degradation, wear property and biocompatibility of nano- $Y_2O_3$ -containing micro-arc oxidation coating on ZK60 alloy

Jun-xiu CHEN<sup>1,2</sup>, Yang YANG<sup>1,2</sup>, Iniobong P. ETIM<sup>3</sup>, Li-li TAN<sup>3</sup>,  
Ke YANG<sup>3</sup>, R. D. K. MISRA<sup>4</sup>, Jian-hua WANG<sup>1,2</sup>, Xu-ping SU<sup>1,2</sup>

1. Key Laboratory of Materials Surface Science and Technology of Jiangsu Province, Changzhou University, Changzhou 213164, China;
2. Jiangsu Collaborative Innovation Center of Photovoltaic Science and Engineering, Changzhou University, Changzhou 213164, China;
3. Institute of Metal Research, Chinese Academy of Sciences, Shenyang 110016, China;
4. Department of Metallurgical, Materials and Biomedical Engineering, University of Texas, El Paso, TX, USA

Received 7 December 2021; accepted 1 April 2022

**Abstract:** In order to further improve the degradation resistance and wear property of micro-arc oxidation (MAO) coating on magnesium alloys, nano- $Y_2O_3$  was added into the electrolyte to fabricate a nano- $Y_2O_3$ -containing MAO coating. Microstructural characterization, wear test, electrochemical test, immersion test and cytotoxicity test were carried out. The results showed that there were mainly  $Ca_8MgY(PO_4)_7$  and  $Y_2O_3$  particles in the MAO coating.  $Ca_8MgY(PO_4)_7$  could stabilize the coating and the nano- $Y_2O_3$  could seal the micro-pores. Therefore, both the degradation resistance and wear property of the coating were improved. The degradation rate decreased from 0.14 to 0.06 mm/a in Hank's solution. The volume loss decreased from 0.46 to 0.27 mm<sup>3</sup> at the same slip distance. MAO coating exhibited good biocompatibility with the cell relative growth rate (RGR) value of more than 90%. The nano- $Y_2O_3$ -containing MAO coating thus has a good promising biomedical application.

**Key words:** nano- $Y_2O_3$ ; MAO coating; wear property; degradation resistance; biocompatibility

## 1 Introduction

At present, the fast degradation rate limits the wide clinical application of magnesium alloys as biodegradable materials [1]. Coating is usually used to improve the corrosion resistance and bioactivity of the magnesium alloys. The commonly used coatings are chemical conversion coating [2], electrodeposited coating [3], organic coating [4] and micro-arc oxidation (MAO) coating [5]. MAO is a promising technique to produce porous and metallurgical bonding coatings on magnesium alloy substrates, and the degradation of magnesium alloys with MAO can be effectively controlled [6–8].

Although MAO coating has good promising application, there are still some shortcomings. In the corrosion process, the structural imperfection in the MAO films enlarges the effective surface areas for corrosion, while the large micro-pores act as the passages for corrosive ions entering into the MAO coatings [9,10]. To overcome the porosity of MAO coatings, sealing treatment is necessary for the MAO coated samples to further improve the corrosion resistance [11–13]. For pure MgO, the pilling bedworth (PB) ratio is inferior to 1 (0.8 [14,15]) indicating that the oxides film cannot completely cover the metal surface. Modification is therefore necessary by some other methods. HU et al [16] found that  $TiO_2$  film fabricated by sol-gel

method could improve the corrosion resistance of AZ31 alloy. CAO et al [17] introduced TiO<sub>2</sub> into the MAO coating of Mg–Zn–Ca alloy and the corrosion current density decreased from  $1.43 \times 10^{-4}$  to  $5.69 \times 10^{-7}$  A/cm<sup>2</sup>. In the case of Y, the PB ratio is greater than 1 (1.39 [18]). Previous studies have found that yttrium (Y) in the corrosion layer of WE43 alloy improves the corrosion resistance of WE43 alloy [19,20]. Moreover, nano-particle reinforcement is a useful method to improve the wear properties of the metals [21,22]. However, there are few studies that demonstrate the effects of nano-Y<sub>2</sub>O<sub>3</sub> on the corrosion resistance and wear property of the MAO coating of magnesium alloy. Therefore, some nano-Y<sub>2</sub>O<sub>3</sub> was added into the electrolyte to fabricate Y<sub>2</sub>O<sub>3</sub>-containing MAO coating on ZK60 alloy in this work. The microstructure, coating adhesion, degradation resistance, wear property and biocompatibility of MAO coating were studied. This would give another method to design high performance MAO coating of Mg alloys.

## 2 Experimental

### 2.1 MAO coating fabrication

The substrate material used in this work was ZK60 alloy with a chemical composition (wt.%) of 5.20 Zn, 3.80 Zr, and balanced Mg. Some samples ( $d12 \text{ mm} \times 3 \text{ mm}$ ) were used for the microstructural observation and immersion test. Other samples ( $d12 \text{ mm} \times 5 \text{ mm}$ ) were molded in epoxy resin for electrochemical test. Grits of 2000<sup>#</sup> sandpapers were used to polish the exposed surface of the samples. A pulsed bipolar electrical source (WHD-20) with a power of 2 kW was used to prepare the MAO coatings. The micro-arc oxidation adopted a constant voltage mode. The working voltage, working frequency, work duty cycle and preparation time were 360 V, 1000 Hz, 40% and 15 min, respectively. The composition of the electrolyte is given in Table 1. After the MAO treatment, the samples were cleaned with distilled water and dried in cold air.

**Table 1** Composition of electrolyte (g/L)

Sample	Ca(OH) <sub>2</sub>	(NaPO <sub>3</sub> ) <sub>6</sub>	KF	Nano-Y <sub>2</sub> O <sub>3</sub>
MAO coating	1.2	4.0	8.0	–
Y <sub>2</sub> O <sub>3</sub> + MAO coating	1.2	4.0	8.0	8.0

### 2.2 Materials characterization

Surface morphologies of MAO coatings were investigated by a scanning electron microscope (SEM) with an energy dispersive X-ray spectroscopy (EDS). The phase compositions of the coatings were analyzed by using X-ray diffractometry (XRD, RIGAKU, D/MAX2500) with Cu K<sub>α</sub> line generated at 40 kV, 150 mA.

### 2.3 Scratch test

The adhesion of the coatings was measured by a multifunctional tester (MFT-4000) at room temperature. The load was continuously loaded to the diamond indenter (the cone angle is 120° and the tip radius is 0.2 mm) through the automatic loading mechanism, and the specimen was moved to make the indenter cross the coating surface. The applied force was set at a speed of 20 N/min at room temperature. The critical load of the adhesion force between the coating and the substrate was obtained by determining the signal of friction change through each sensor. All the measurements were repeated three times.

### 2.4 Wear test

The wear test was carried out by a tribometer (CSM Instruments). A 5 N linear force was applied horizontally in a forward and backward direction, covering a track of 10 mm on the sample. Silicon nitride ball was used for the friction test. The highest speed and frequency of the electric motor was 12.5 cm/s and 2 Hz, respectively. The test was carried out three times for each coating. After the round-trip friction distance reached 100 m, the wear volume loss ( $W$ ) was calculated as [23]

$$W=AL \quad (1)$$

where  $A$  is the cross-section area (mm<sup>2</sup>) of the wear track which is measured by using a surface profile measurement instrument (Alpha-Step IQ), and  $L$  (mm) is the length of the track.

### 2.5 Electrochemical measurements

A Gamry Instrument (Reference 600+) was used to perform the electrochemical test. The samples were set as the working electrode. A saturated calomel electrode (standard potential of 0.2412 V at 25 °C) was set as a reference electrode. A platinum electrode was set as the counter electrode. The samples were immersed into a 37 °C

Hank's solution [24]. First, open circuit potential (OCP) was measured for 1800 s. Then, the electrochemical impedance spectroscopy (EIS) experiment was performed at the open circuit potential. The frequency range was  $10^5$ –0.01 Hz. Finally, the potentiodynamic polarization curve was measured from  $-0.25$  to  $0.35$  V with reference to the OCP. The scan rate was  $0.5$  mV/s. Under each testing condition, the test was repeated three times in order to guarantee reliability and reproducibility.

## 2.6 Immersion test

Samples ( $d10$  mm  $\times$  3 mm) were immersed in Hank's solution for 14 d. The ratio of sample surface area ( $\text{cm}^2$ ) to solution volume (mL) was 1.25 according to ISO 10993–12 standard. The samples were put into 10 mL centrifugal tube. The surface area of the sample was  $3.39$   $\text{cm}^2$  and the volume of solution was  $2.7$  mL. The Hank's solution was changed every day in order to keep it fresh and the solution pH variation was recorded during the entire immersion period [24]. After immersion, the samples were cleaned in chromium trioxide solution to remove the corrosion products. The corrosion morphology of the alloy was observed by SEM and a laser confocal scanning microscope (LSM 700).

## 2.7 Cytocompatibility test

Human osteosarcoma cells (MG63) were used to evaluate the cytotoxicity of the alloys. They were cultured in Dulbecco's modified Eagle's medium (DMEM) with 10% fetal bovine serum (FBS) and some antibiotics including 100 mg/mL streptomycin and 100 U/mL penicillin at  $37$  °C in a humidified atmosphere of 5%  $\text{CO}_2$ . The samples extract was prepared using DMEM serum free medium with the immersion ratio of  $1.25$   $\text{cm}^2/\text{mL}$  in a humidified atmosphere with 5%  $\text{CO}_2$  at  $37$  °C for 24 h, and subsequently, the supernatant was collected and filtered by a  $0.22$   $\mu\text{m}$  filter. Cells were incubated in 96-well plates at  $1 \times 10^4$  cells/mL medium for 24 h. The control group with only DMEM medium was the negative control and the DMEM medium with 10% DMSO was the positive control. The medium was then replaced with 100  $\mu\text{L}$  of extract. After 1, 3 and 5 d, MTT (10  $\mu\text{L}$ ) was added to each well and the samples were incubated with MTT (3-(4,5)-dimethylthiazazo(-z-yl)-3,5-diphenyl-tetrazolium bromide) at  $37$  °C for 4 h, and then

150  $\mu\text{L}$  dimethylsulfoxide (DMSO) was added in each well. The optical density (OD) values were measured by a microplate reader at 490 nm with a reference wavelength of 570 nm. The cell relative growth rate (RGR) was calculated according to [24]

$$\text{RGR} = \text{OD}_{\text{test}} / \text{OD}_{\text{negative}} \times 100\% \quad (2)$$

## 3 Results

### 3.1 Microstructure

Figure 1 presents the microstructures of the cross-section and surface of the two coatings. It can be seen that the thickness of MAO coating and  $\text{Y}_2\text{O}_3$  + MAO coatings were 4–11 and 3–10  $\mu\text{m}$  (Figs. 1(a) and (b)), respectively. From the cross-sectional morphologies, more micro-pores were observed in MAO coating than in  $\text{Y}_2\text{O}_3$  + MAO coating. From surface morphologies, many uniformly distributed micro-pores with diameter of 2  $\mu\text{m}$  on the MAO coating were observed (Fig. 1(c)). However, the diameter of micro-pores on the  $\text{Y}_2\text{O}_3$  + MAO coating was obviously decreased to 1  $\mu\text{m}$ . It can be seen from EDS results of Regions A and B (Figs. 1(e, f)) that relatively compact  $\text{MgF}_2$  layer was formed in Region A [25], while  $\text{Y}_2\text{O}_3$  particles were the main components in Region B. Figure 2 presents the XRD patterns of the coatings. For the uncoated alloy, the main second phases were  $\alpha$ -Mg and  $\text{MgZn}_2$ . The main compositions were  $\alpha$ -Mg, MgO and  $\text{Mg}_3(\text{PO}_4)_2$  in the MAO coating. For the  $\text{Y}_2\text{O}_3$  + MAO coated samples, apart from the above composition, there were still some  $\text{Y}_2\text{O}_3$  and  $\text{Ca}_8\text{MgY}(\text{PO}_4)_7$ .

### 3.2 Scratch test results

There was a sudden change of the friction coefficient before it reached stable friction stage. The critical scratch force could be judged according to the sudden change in the friction coefficient. Therefore, the adhesion of the coating could be obtained from Fig. 3. For the MAO coated samples, the critical force was  $(4.50 \pm 0.35)$  N (Fig. 3(a)). For the  $\text{Y}_2\text{O}_3$  + MAO coated samples, the critical force was  $(6.03 \pm 0.25)$  N (Fig. 3(b)). Compared with MAO coated samples, the critical force of  $\text{Y}_2\text{O}_3$  + MAO coated samples was increased obviously, indicating that the addition of  $\text{Y}_2\text{O}_3$  could improve the adhesion of the coating. The reason for the difference in the initial applied force (0–6 N) may be that the micro-surface of the two coatings were

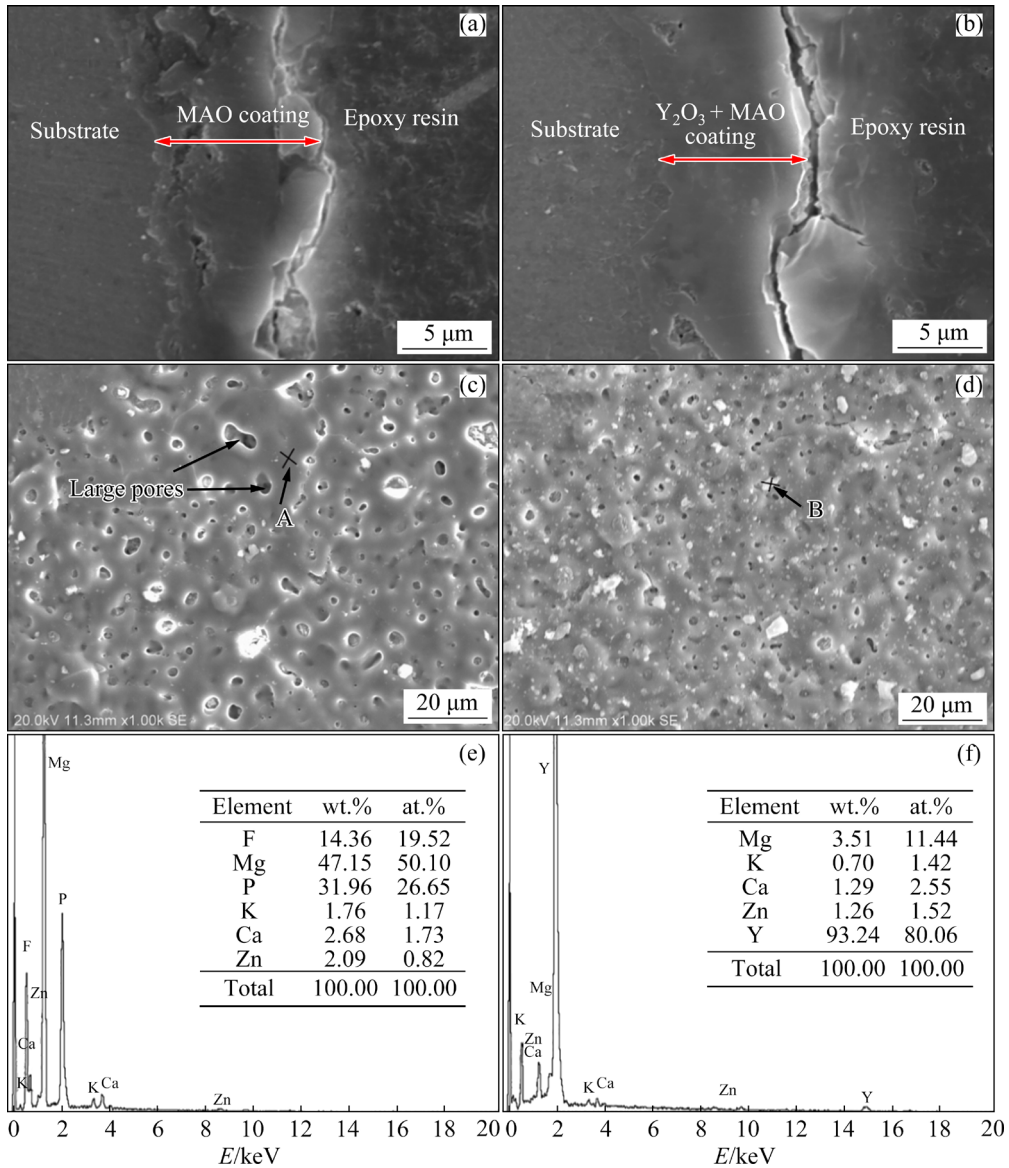


**Fig. 1** Microstructures of MAO coating (a, c) and  $Y_2O_3$  + MAO coating (b, d), and EDS results of Regions A (e) and B (f): (a, b) Cross-sectional morphologies; (c, d) Surface morphologies

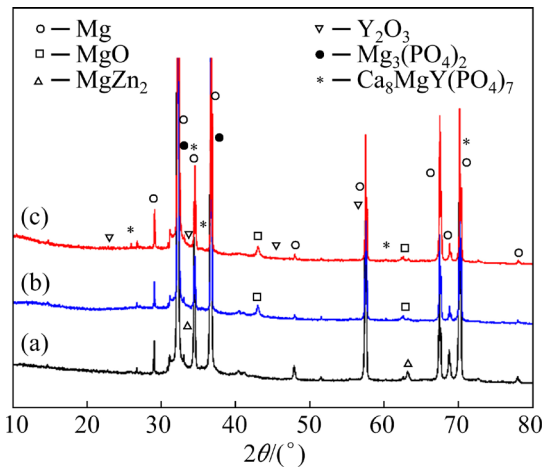


**Fig. 2** XRD patterns of coatings: (a) Uncoated; (b) MAO coating; (c)  $Y_2O_3$  + MAO coating

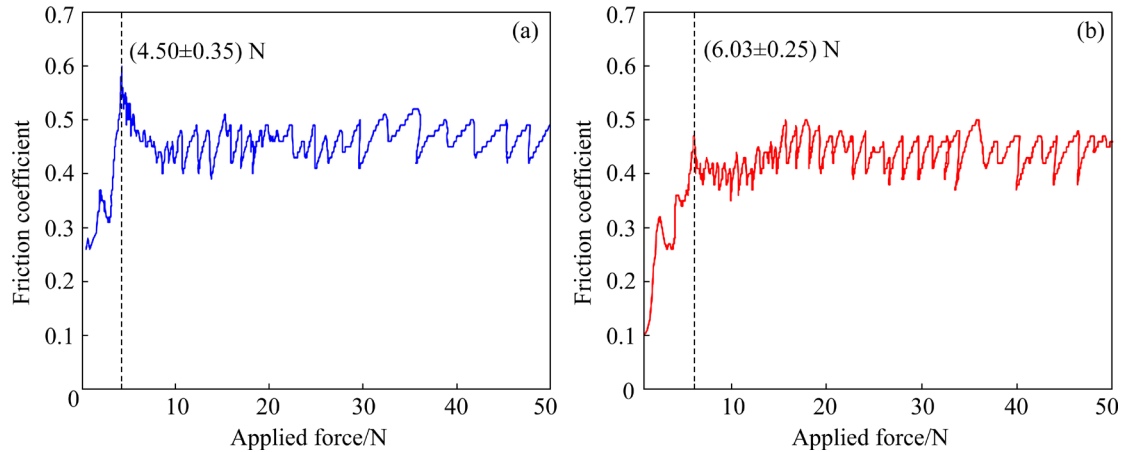
uneven, and the applied force was not homogeneous at the initial stage.

### 3.3 Wear property

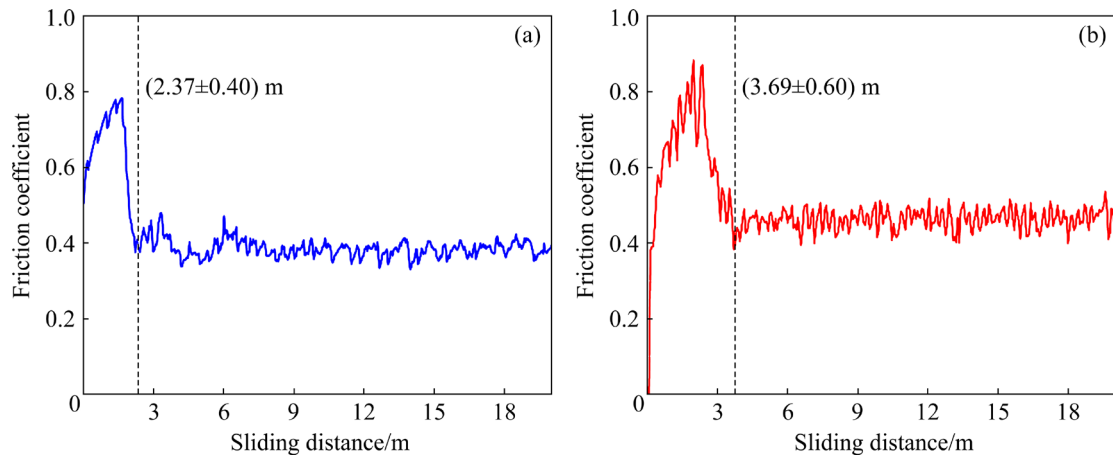
Figure 4 presents the relationship between the friction coefficient and the sliding distance. A significant change in the friction coefficient was observed when the coatings were destroyed and then the friction coefficient stabilized at about 0.4. The sliding distance before the coating was completely destroyed, and this can be inferred according to the huge shift of changing point. The  $Y_2O_3$  + MAO coating had the longer sliding distance ((3.69±0.60) m) than the MAO coating ((2.37±0.40) m). This indicates that  $Y_2O_3$  + MAO

coating had better wear property. Figure 5 and Table 2 respectively present the typical cross-sectional profile of the wear tracks and the volume loss of the coated alloys. Since the length of the track was the same (10 mm), the volume losses of the coated alloys were calculated according to Eq. (1). The volume loss of uncoated alloy, MAO coated alloy,  $Y_2O_3$  + MAO coated alloy were 0.72, 0.46 and 0.27  $mm^3$ , respectively. Therefore, it could

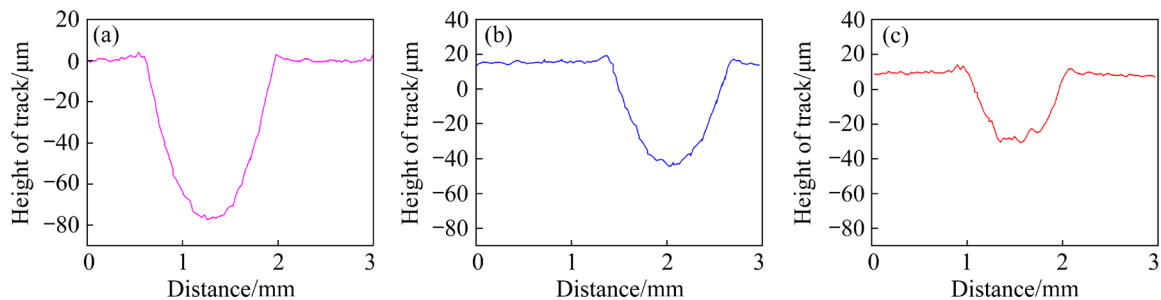
be seen that  $Y_2O_3$  + MAO coating had the better protective effect than MAO coating. Figure 6 shows the morphologies of the tracks after friction. It can be seen that the width of the tracks of the  $Y_2O_3$  + MAO coating was smaller than that of MAO coating (Figs. 6(a, c)). In addition, the damage area of the coating was different. The widths of damage of MAO coating and  $Y_2O_3$  + MAO coatings were about 80–118 and 46–77  $\mu m$ , respectively (Figs. 6(b, d)).



**Fig. 3** Relationship between applied force and friction coefficient: (a) MAO coated sample; (b)  $Y_2O_3$  + MAO coated sample



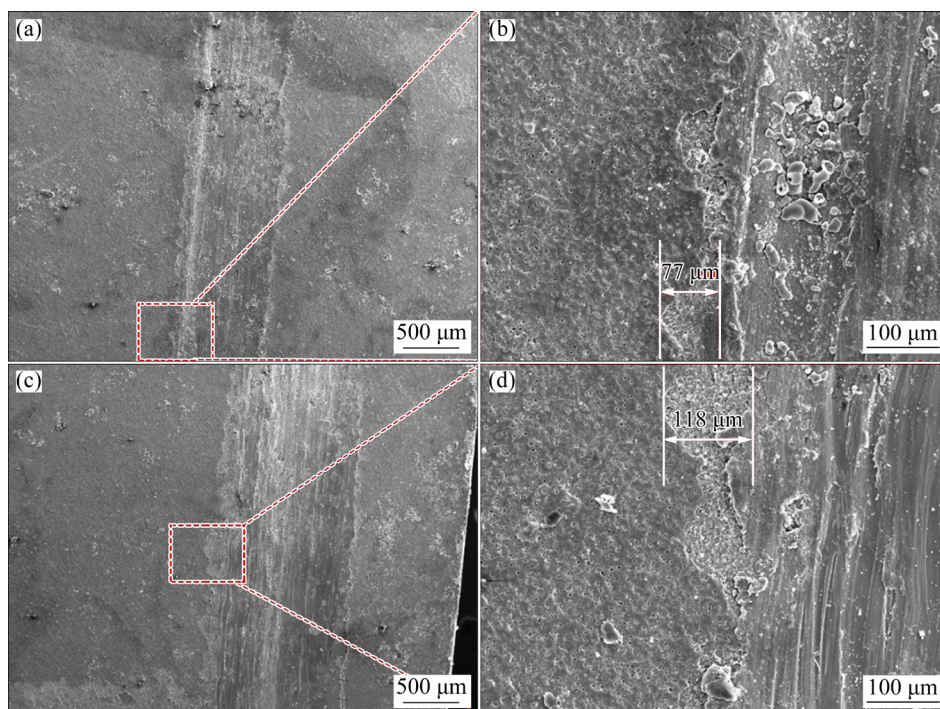
**Fig. 4** Relationship between sliding distance and friction coefficient: (a) MAO coated sample; (b)  $Y_2O_3$  + MAO coated sample



**Fig. 5** Typical cross-sectional profile of wear tracks after 100 m friction: (a) Uncoated sample; (b) MAO coated sample; (c)  $Y_2O_3$  + MAO coated sample

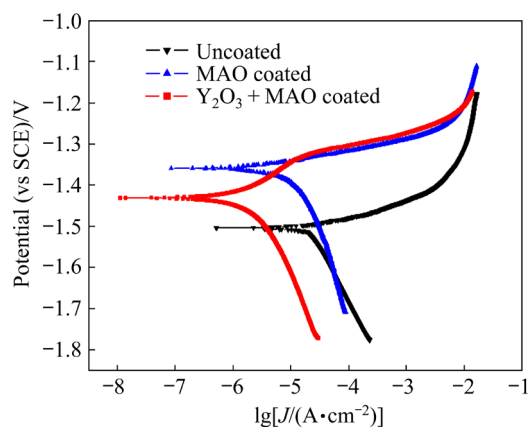
**Table 2** Parameters of wear tracks of samples after 100 m friction

Sample	Maximum depth/ $\mu\text{m}$	Area of track/ $\text{mm}^2$	Volume loss/ $\text{mm}^3$
Uncoated	$78\pm 3$	$0.0720\pm 0.0016$	$0.720\pm 0.016$
MAO coated	$61\pm 3$	$0.0460\pm 0.0022$	$0.460\pm 0.022$
$\text{Y}_2\text{O}_3$ + MAO coated	$43\pm 4$	$0.0270\pm 0.0018$	$0.270\pm 0.018$

**Fig. 6** Morphologies of tracks after friction: (a, b)  $\text{Y}_2\text{O}_3$  + MAO coating; (c, d) MAO coating

### 3.4 Electrochemical property

Figure 7 shows potentiodynamic polarization results of the samples. For the coated samples, the curves shifted to the left, signifying that the corrosion current density decreased. The Tafel fitting results of the potentiodynamic curves are given in Table 3. The corrosion current density ( $J_{\text{corr}}$ ) was closely related to the corrosion resistance

**Fig. 7** Potentiodynamic polarization curves of samples in Hank's solution**Table 3** Tafel fitting results based on potentiodynamic polarizations tests in Hank's solution

Sample	$J_{\text{corr}}/(\mu\text{A}\cdot\text{cm}^{-2})$	$\varphi_{\text{corr}}(\text{vs SCE})/\text{V}$	Corrosion rate/ $(\text{mm}\cdot\text{a}^{-1})$
Uncoated	$25.60\pm 2.20$	$-1.50\pm 0.01$	$0.58\pm 0.05$
MAO coated	$6.32\pm 1.50$	$-1.36\pm 0.02$	$0.14\pm 0.03$
$\text{Y}_2\text{O}_3$ + MAO coated	$2.75\pm 0.75$	$-1.43\pm 0.01$	$0.06\pm 0.02$

of the samples. The higher the  $J_{\text{corr}}$ , the larger the degradation rate of the sample. The values of  $J_{\text{corr}}$  of the uncoated, MAO coated and  $\text{Y}_2\text{O}_3$  + MAO coated samples were 25.60, 6.32 and 2.75  $\mu\text{A}/\text{cm}^2$ , respectively. Similarly, the degradation rates were 0.58, 0.14 and 0.06 mm/a, respectively. When  $\text{Y}_2\text{O}_3$  was added, the corrosion resistance was improved by 2 and 10 times as compared with the MAO coated and uncoated samples, respectively. Also, it can be found that the potential of the coated samples was higher than that of the uncoated ones. It was also reflected that the coating reduced the tendency of the alloy to be corroded.

Figure 8 presents the impedance curves of the samples. Equivalent circuits of EIS curves of uncoated and coated samples are shown in Figs. 8(d, e), respectively. For uncoated samples, there are mainly three parts in the equivalent circuit. The first part is a solution resistance  $R_s$ . The second part involves a film resistance  $R_1$  in parallel with constant-phase element  $CPE_1$ , which represents the capacitance loop in high frequency. The last part contains a charge transfer resistance  $R_2$  in parallel with  $CPE_2$ , which represents the capacitance loop in medium frequency. An inductance  $L$  in series with  $R_3$  are used to describe the low frequency inductance loop, indicating hydrogen evolution on

the surface of the substrate. The low-frequency inductance ring indicates that the corrosive medium has reached the substrates and represents the beginning of pitting. For the coated sample, the circuit does not contain a low frequency inductor loop. Constant-phase element (CPE) is used in place of a capacitor to compensate the non-homogeneity, which is defined by two values,  $Y$  and  $n$ .  $n$  is a CPE exponent which provides a measure of the unevenness of the electrode surface. When  $n$  is equal to 1, CPE behaves like an ideal capacitor. The fitting results are shown in Table 4. The  $R_1$  value of  $Y_2O_3 + MAO$  coated samples was much larger than that of MAO coated samples and uncoated samples,

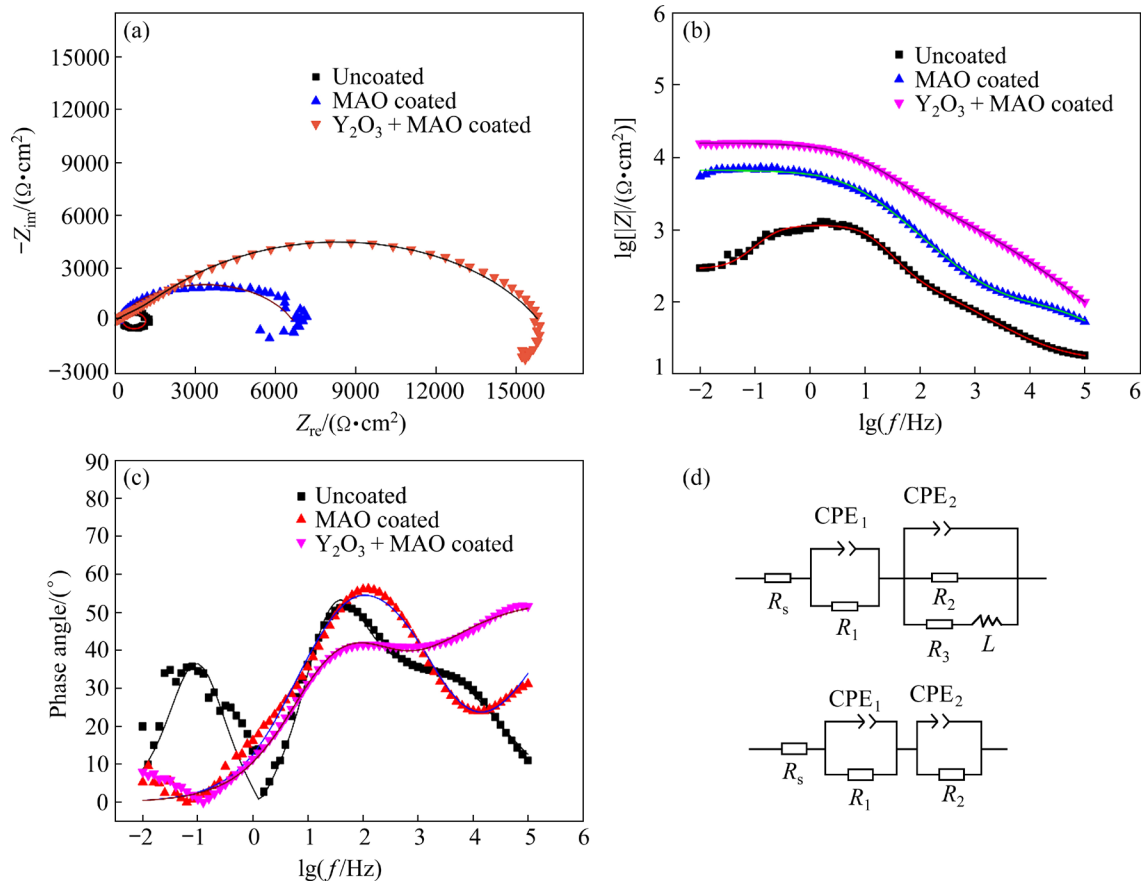


**Fig. 8** Impedance curves: (a) Nyquist curves; (b) Bode curves; (c) Bode phase angle curves; (d) Equivalent circuit of uncoated samples; (e) Equivalent circuit of coated samples

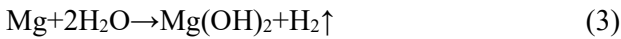
**Table 4** Fitting results of alloy from impedance curves in Hank’s solution

Sample	$R_s/$ ( $\Omega \cdot \text{cm}^2$ )	$CPE_1$		$R_1/$ ( $\Omega \cdot \text{cm}^2$ )	$CPE_2$		$R_2/$ ( $\Omega \cdot \text{cm}^2$ )	$R_3/$ ( $\Omega \cdot \text{cm}^2$ )	$L/$ ( $\text{H} \cdot \text{cm}^{-2}$ )
		$Y_{01}/$ ( $\mu\Omega^{-1} \cdot \text{cm}^{-2} \cdot \text{s}^{-1}$ )	$n_1$		$Y_{02}/$ ( $\mu\Omega^{-1} \cdot \text{cm}^{-2} \cdot \text{s}^{-1}$ )	$n_2$			
Untreated	14.63	72.98	0.60	147.9	13.91	0.99	981.3	144.5	945.3
MAO coated	30.81	1.82	0.66	90.71	11.58	0.70	$8.43 \times 10^3$	–	–
$Y_2O_3 + MAO$ coated	31.27	5.46	0.60	$1.01 \times 10^3$	4.82	0.70	$1.60 \times 10^4$	–	–

indicating that the  $Y_2O_3 + MAO$  coating provided a great protective effect on the substrates. For the coated sample, although the corrosion media gradually migrated inward, the dense inner layer continued to provide protection for the substrate because  $R_2$  was greater than  $R_1$ . For the uncoated sample, the corrosion products formed in the inner layer resisted the diffusion of aggressive ions inward [26].

**3.5 Immersion test results**

The pH change of the Hank’s solution is presented in Fig. 9. For the uncoated sample, during the 14 d immersion, the pH value was very stable at about 10.7. For the coated samples, at the initial immersion stage, the pH value of the solution increased rapidly and then decreased gradually. After 5 d, the pH of the solution was stable. When coated samples were immersed into the solution, the surface area of the sample could react with the solution immediately, leading to increased alkalinity of the solution. The decrease in the surface area also decreased the reaction. Moreover, when the corrosion process was inhibited, the dissolution process of Mg was also inhibited:



There would be less hydroxyl ions generated; therefore, the pH value of the solution decreased. Until 5 d immersion, the corrosion process was stable. After immersion, the samples were taken out and washed with chromic acid solution and the topography of the samples were observed (Fig. 10). For the uncoated samples, there were some deep pits observed. The alloy was severely corroded. For the MAO coated samples, the number of the deep

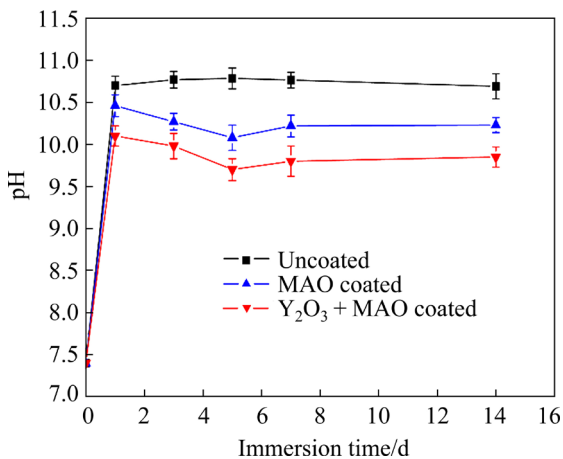


**Fig. 9** pH change of Hank’s solution for 14 d immersion

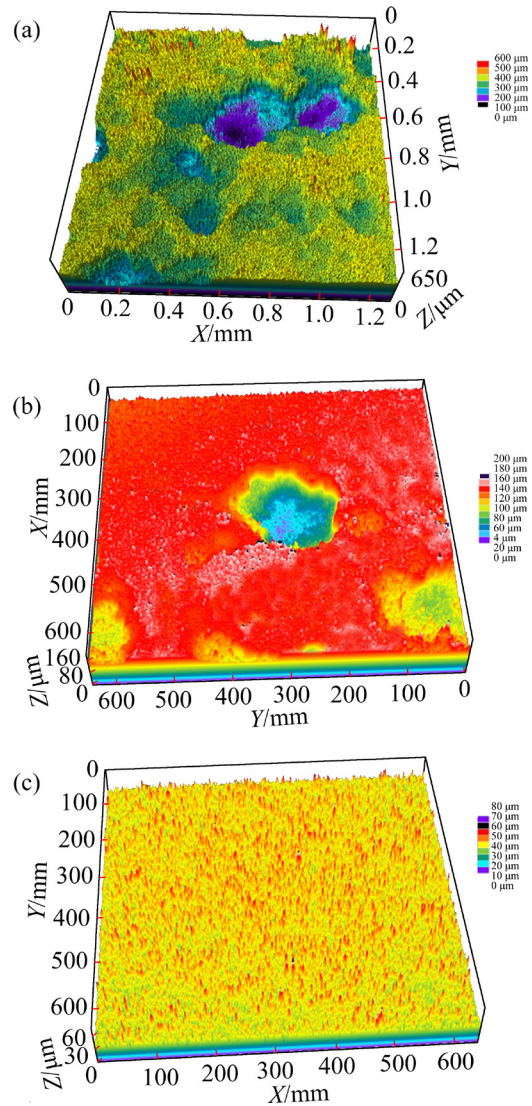


**Fig. 10** Topographies of samples observed by laser confocal scanning microscope after removal of degradation products: (a) Uncoated sample; (b) MAO coated sample; (c)  $Y_2O_3 + MAO$  coated sample

pits obviously decreased. However, for the  $Y_2O_3 + MAO$  coated samples, there was virtually no deep pits observed, as they exhibited relatively uniform corrosion. The depth difference  $R_{max}$  and the surface roughness  $R_a$  are the two important parameters used to evaluate the samples corrosion morphologies. They are illustrated in Table 5. The values of  $R_{max}$  and  $R_a$  of the  $Y_2O_3 + MAO$  coated sample were the lowest also reflecting the addition of  $Y_2O_3$  to improve the corrosion resistance of the coating. Figure 11 shows the corrosion morphologies of the samples. For the uncoated sample, the corrosion products were large and non-uniform. After the corrosion products were removed, deep corrosion

**Table 5** Depth difference and surface roughness of samples

Sample	Depth difference, $R_{max}/\mu\text{m}$	Surface roughness, $R_a/\mu\text{m}$
Uncoated	411	71
MAO coated	147	21
$\text{Y}_2\text{O}_3$ + MAO coated	20	5

pits were observed. For the MAO coated sample, the corrosion products were much more uniform than those of the uncoated samples; however, they were not compact. After the corrosion layer was removed, many corrosion pits could also be observed. For the  $\text{Y}_2\text{O}_3$  + MAO coated sample, the corrosion products were more compact than those of the MAO coated. After the corrosion products were removed, no deep corrosion pits were observed. Figure 12 presents the XRD patterns of the corrosion products of the coated samples after 14 d immersion. For the MAO coating, the main corrosion products were  $\text{Mg}(\text{OH})_2$  and  $\text{MgO}$ ; for  $\text{Y}_2\text{O}_3$  + MAO coating, except  $\text{Mg}(\text{OH})_2$  and  $\text{MgO}$ ,  $\text{Ca}_8\text{MgY}(\text{PO}_4)_7$  was also observed, indicating that  $\text{Ca}_8\text{MgY}(\text{PO}_4)_7$  could protect substrates well.

### 3.6 Cytocompatibility

Figure 13 illustrates the cell viability after co-culturing with extracts for 1, 3 and 5 d. For all the cells, the RGR values increased with an increase in the incubation time. For the uncoated sample, the RGR value increased from 81% to 84%; for the

MAO coated sample, the RGR value increased from 90% to 92%; for the  $\text{Y}_2\text{O}_3$  + MAO coated sample, RGR value increased from 91% to 93%. The coated samples showed better biocompatibility than the uncoated sample. However, no significant difference was observed between the two kinds of coatings.

## 4 Discussion

### 4.1 Effects of nano- $\text{Y}_2\text{O}_3$ on wear property of MAO coating

Nowadays, nano-particle reinforcement to improve the wear property of metals is widely studied [27,28]. When the particles are uniformly distributed in the substrates, they could obviously improve the wear property of the substrates. Coating is an effective method to improve the wear resistance of Mg alloys [29]. According to CHEN et al [30], MAO coating was easily destroyed from the micro-pores during the friction process. The mechanism of  $\text{Y}_2\text{O}_3$  improving the wear property of MAO coating can be summarized as follows.

There were many micro-pores in the MAO coating, which was detrimental to wear property. During the micro-arc oxidation process, when the Mg alloy dissolved,  $\text{Mg}^{2+}$  reacted with  $\text{F}^-$ ,  $\text{OH}^-$  and  $\text{PO}_4^{3-}$  to form  $\text{MgF}_2$ ,  $\text{Mg}(\text{OH})_2$  and  $\text{Mg}_3(\text{PO}_4)_2$ , respectively [31]. Some  $\text{Y}_2\text{O}_3$  nanoparticles combined with these reaction products, leading to their absorption on the Mg alloy surface. Some of

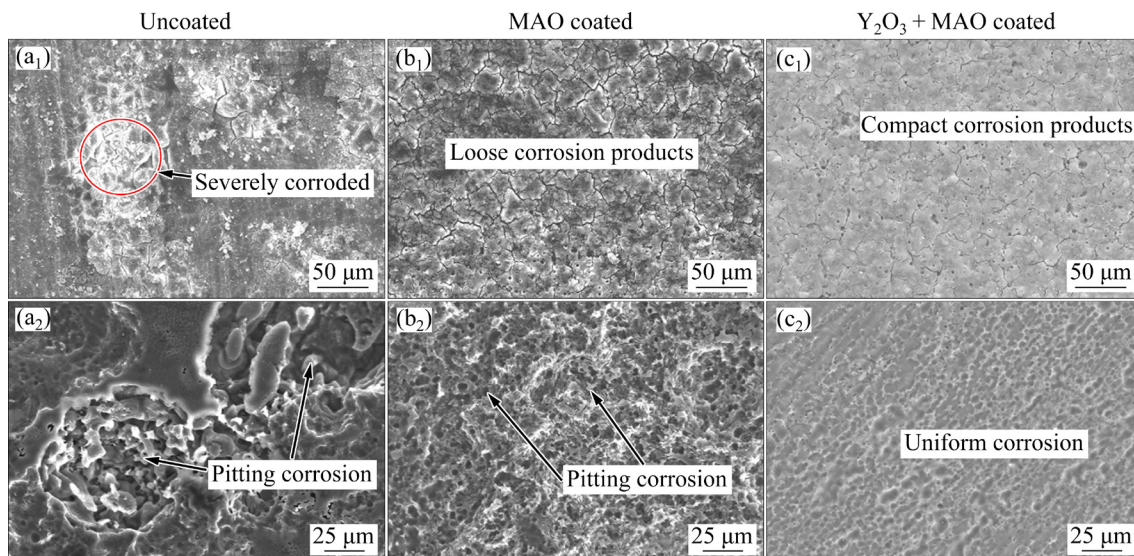


**Fig. 11** Corrosion morphologies of samples: (a<sub>1</sub>, b<sub>1</sub>, c<sub>1</sub>) With corrosion products; (a<sub>2</sub>, b<sub>2</sub>, c<sub>2</sub>) With corrosion products removed

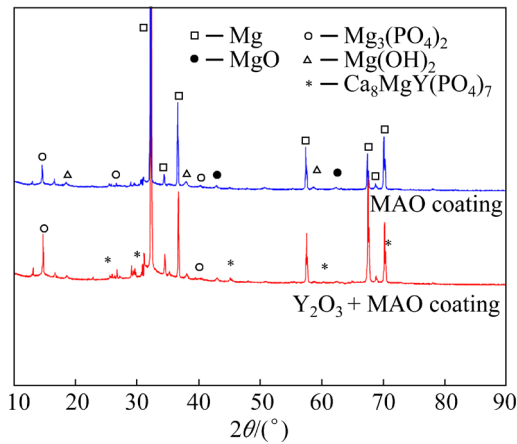


**Fig. 12** XRD patterns of coatings after 14 d immersion in Hank's solution

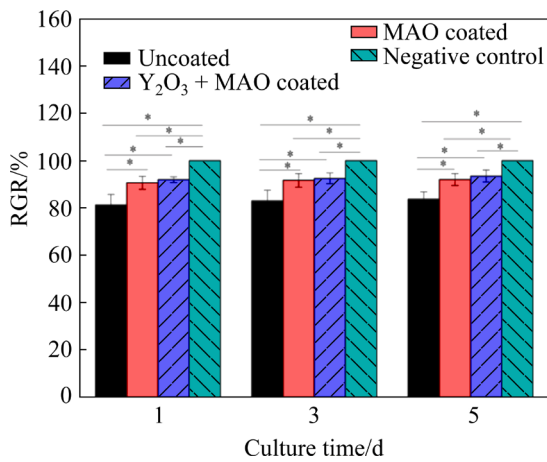
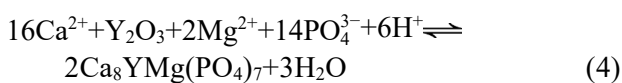


**Fig. 13** Cell viabilities after incubation with different extracts for different time (\* $P > 0.05$  mean that the difference is not significant)

them got deposited into the micro-pores, leading to a decrease in pore diameter or even its disappearance. This suggests that the amount of crack source in the MAO coating reduced during the friction. Thus, the coating was not destroyed from the micro-pores. Moreover, some of the yttrium had a reaction with calcium ( $\text{Ca}^{2+}$ ) and phosphate ( $\text{PO}_4^{3-}$ ) to form  $\text{Ca}_8\text{MgY}(\text{PO}_4)_7$  that could reinforce the coating, keeping its integrity. The reaction was deduced as.



The friction particles were not easily separable from the MAO coating. This means except for the micro-pores, the other parts of the coating were also stable, and not easily destroyable. Besides, the addition of  $\text{Y}_2\text{O}_3$  also improved the MAO coating

adhesion with the substrates. The critical scratch force improved from 4.50 to 6.03 N. This means the  $\text{Y}_2\text{O}_3$  + MAO coating had better adhesion with the substrates. It could not be easily peeled off from the substrates. The reason why the addition of  $\text{Y}_2\text{O}_3$  could improve the adhesion could be explained as follows. From the observation of microstructure of the cross section of the two coatings, there were many micro-pores in the interfaces between the substrate and the MAO coating. However, almost no pores were observed in the interfaces between the substrate and the MAO coating. When there were many pores, the adhesion between the coating and the substrate was decreased. Thus, the critical scratch force also decreased. The effects of  $\text{Y}_2\text{O}_3$  on the wear properties of MAO coating were as follows: reducing micro-pores, particle reinforcement and enhancing adhesion between coating and substrates.

#### 4.2 Effects of nano- $\text{Y}_2\text{O}_3$ on degradation behaviors of MAO coating

MAO coating usually corrode from the micro-pores. Many researchers put their attention on the fabrication of MAO composite coating in order to solve this issue. The composite coatings were mainly made up of MAO/sol-gel coating [32], MAO/electrodeposition coating [33], MAO/poly(lactic acid) (PLA) coating [34], etc. Although these methods could improve the degradation resistance of the MAO coating, it takes much time and increases the costs. In this work, nano- $\text{Y}_2\text{O}_3$  was added into the electrolyte to fabricate nano- $\text{Y}_2\text{O}_3$ -containing MAO coating and the coating degradation resistance was improved. The corresponding mechanism was concluded as follows.

On one hand, for the MAO coating, there were many micro-pores in the coating (Fig. 14(a)), and corrosion easily occurred from the pores leading to pitting corrosion due to the galvanic effect between the second phases and the substrate [35]. The coating was peeled off into the solution (Fig. 14(c)).  $\text{Y}_2\text{O}_3$  reacted with the electrolyte to form  $\text{Ca}_8\text{MgY}(\text{PO}_4)_7$  and deposited in the MAO coating. Y is an inert element. Nano- $\text{Y}_2\text{O}_3$ -containing compounds could stabilize the coating. When MAO coating was corroded, it could not be easily peeled off from the substrates. Moreover, according to previous report [19], some Y elements could

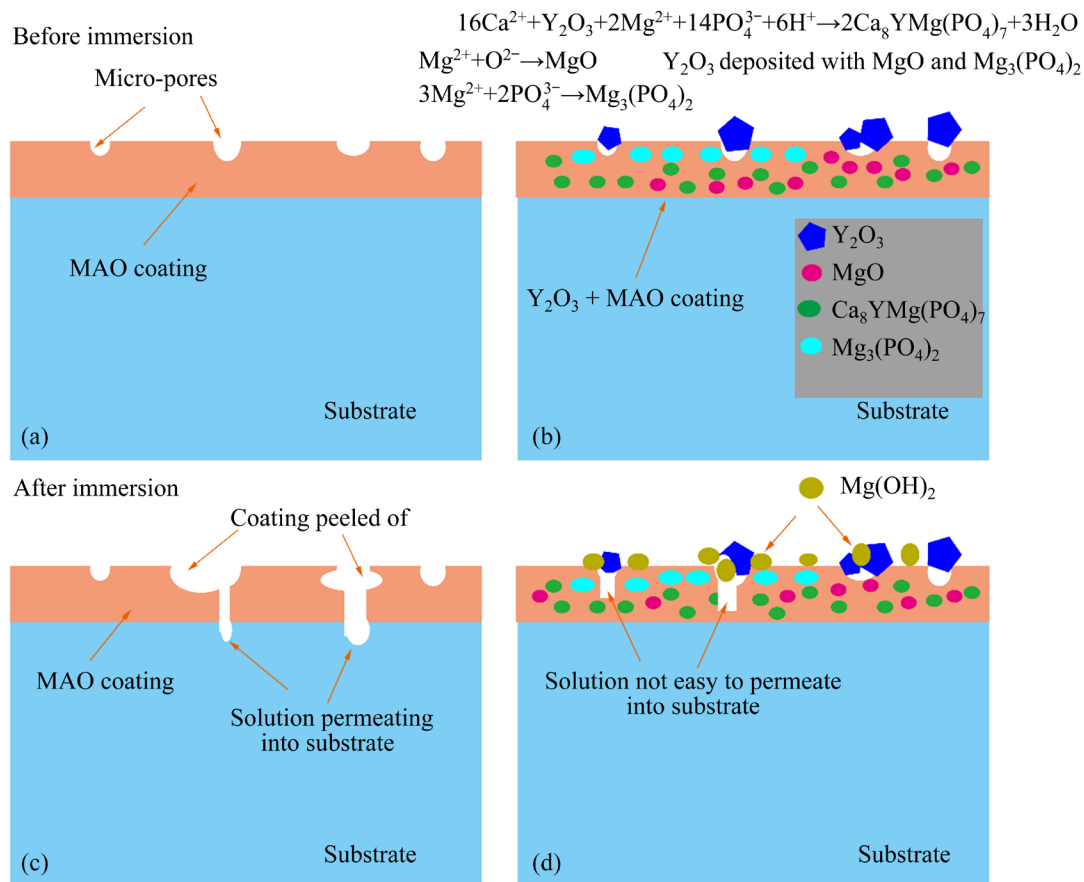


**Fig. 14** Schematic illustration of degradation of coatings: (a, c) MAO coating; (b, d)  $\text{Y}_2\text{O}_3 + \text{MAO coating}$

dissolve into the corrosion products and stabilize them. Therefore, the degradation resistance was improved. On the other hand, there were some  $\text{Y}_2\text{O}_3$  particles deposited in the micro-pores, and the number and the size of the micro-pores were reduced. The micro-pores were sealed due to the addition of the  $\text{Y}_2\text{O}_3$  particles (Fig. 14(b)). Besides, the corrosion products such as  $\text{Mg}(\text{OH})_2$  could deposit in the corroded pores, which could inhibit the corrosion process (Fig. 14(d)). Therefore,  $\text{Y}_2\text{O}_3 + \text{MAO coating}$  could protect the substrates better with the degradation rate decreasing from 0.14 to 0.06 mm/a in Hank's solution

#### 4.3 Effects of nano- $\text{Y}_2\text{O}_3$ on biocompatibility of MAO coating

It was reported that MgYREZr alloy (similar to WE43 alloy) had better biocompatibility [36] and the yttrium element content in the blood was still within the reference range [37]. For the uncoated sample, the content of  $\text{Mg}^{2+}$  ions was relatively high due to its fast degradation. Moreover, the alkalinity of the solution increased. These two aspects led to

the decrease of the biocompatibility of the sample. The RGR value was just about 80%. For the coated sample, the fast degradation rate was inhibited. The content of  $\text{Mg}^{2+}$  ions and pH value of the solution were much lower. Besides, there were some beneficial elements such as Ca and P dissolved into the solution; therefore, the RGR value was more than 90%, exhibiting good biocompatibility. The addition of  $\text{Y}_2\text{O}_3$  did not affect the coating biocompatibility. The RGR value could still maintain more than 90%. Moreover, no significant difference was observed between the two kinds of coatings.

## 5 Conclusions

(1) There were mainly  $\text{Ca}_8\text{MgY}(\text{PO}_4)_7$  and  $\text{Y}_2\text{O}_3$  particles in the coating. They could stabilize the coating and the nano- $\text{Y}_2\text{O}_3$  could seal the micro-pores. Therefore, the degradation resistance of the coating was improved.

(2) The addition of  $\text{Y}_2\text{O}_3$  improved the wear property of the MAO coating. This was related to

the decrease of the micro-pores, particle reinforcement and enhancement of the coating adhesion with the substrates.

(3) The addition of  $Y_2O_3$  did not decrease the biocompatibility of the MAO coating. The RGR value could reach more than 90%, showing good cell viability.

## Acknowledgments

This work was supported by the National Natural Science Foundation of China (Nos. 52001034, 51871030), Changzhou Sci & Tech Program, China (No. CJ20200078), Natural Science Foundation of Jiangsu Higher Education Institutions of China (No. 20KJB430013), the Top-notch Academic Programs of Jiangsu Higher Education Institutions, China (TAPP) and the Priority Academic Program Development of Jiangsu Higher Education Institutions, China (PAPD).

## References

- [1] MAKKAR P, KANG H J, PADALHIN A R, FARUQ O, LEE B. In-vitro and in-vivo evaluation of strontium doped calcium phosphate coatings on biodegradable magnesium alloy for bone applications [J]. *Applied Surface Science*, 2020, 510: 145333.
- [2] ZAI W, ZHANG X R, SU Y C, MAN H C, LI G Y, LIAN J S. Comparison of corrosion resistance and biocompatibility of magnesium phosphate (MgP), zinc phosphate (ZnP) and calcium phosphate (CaP) conversion coatings on Mg alloy [J]. *Surface & Coatings Technology*, 2020, 397: 125919.
- [3] KHAZENI D, SAREMI M, SOLTANI R. Development of HA-CNTs composite coating on AZ31 magnesium alloy by cathodic electrodeposition. Part 1: Microstructural and mechanical characterization [J]. *Ceramics International*, 2019, 45: 11174–11185.
- [4] JOTHI V, ADESINA A Y, KUMAR A.M, RAHMAN M M, RAM J S N. Enhancing the biodegradability and surface protective performance of AZ31 Mg alloy using polypyrrole/gelatin composite coatings with anodized Mg surface [J]. *Surface & Coatings Technology*, 2020, 381: 125139.
- [5] YAN X D, ZHAO M C, YANG Y, TAN L L, ZHAO Y C, YIN D F, YANG K, ATRENS A. Improvement of biodegradable and antibacterial properties by solution treatment and micro-arc oxidation (MAO) of a magnesium alloy with a trace of copper [J]. *Corrosion Science*, 2019, 156: 125–138.
- [6] DOU J H, WANG J, LU Y P, CHEN C Z, YU H J, MA R L W. Bioactive MAO/CS composite coatings on Mg–Zn–Ca alloy for orthopedic applications [J]. *Progress in Organic Coatings*, 2021, 152: 106112.
- [7] ZHU Ji-yuan, JIA Hao-jie, LIAO Kai-jin, LI Xian-xuan. Improvement on corrosion resistance of micro-arc oxidized AZ91D magnesium alloy by a pore-sealing coating [J]. *Journal of Alloys and Compounds*, 2021, 889: 161460.
- [8] LIN Jiu-zao, CHEN Wei-dong, TANG Qiang-qiang, CAO Luo-yuan, SU Sheng-hui. Lithium-modified MAO coating enhances corrosion resistance and osteogenic differentiation for pure magnesium [J]. *Surfaces Interfaces*, 2021, 22: 100805.
- [9] ZHANG Ju-mei, WANG Kai, DUAN Xin, ZHANG Yang, CAI Hui, WANG Zhi-hu. Effect of hydrothermal treatment time on microstructure and corrosion behavior of micro-arc oxidation/layered double hydroxide composite coatings on LA103Z Mg–Li alloy in 3.5 wt.% NaCl solution [J]. *Journal of Materials Engineering and Performance*, 2020, 29: 4032–4039.
- [10] CHEN Jun-feng, LIANG Si-yan, FU Dian-bao, FAN Wang-xian, LIN Wen-xin, REN Wei-wei, ZOU Lin-chi, CUI Xi-ping. Design and in situ prepare a novel composite coating on Mg alloy for active anti-corrosion protection [J]. *Journal of Alloys and Compounds*, 2020, 831: 154580.
- [11] CHU C L, HAN X, XUE F, BAI J, CHU P K. Effects of sealing treatment on corrosion resistance and degradation behavior of micro-arc oxidized magnesium alloy wires [J]. *Applied Surface Science*, 2013, 271: 271–275.
- [12] CHEN J X, ZHANG Y, IBRAHIM M, ETIM I P, TAN L L, YANG K. In vitro degradation and antibacterial property of a copper-containing micro-arc oxidation coating on Mg–2Zn–1Gd–0.5Zr alloy [J]. *Colloids and Surfaces B: Biointerfaces*, 2019, 179: 77–86.
- [13] DONG Kai-hui, SONG Ying-wei, SHAN Da-yong, HAN En-hou. Corrosion behavior of a self-sealing pore micro-arc oxidation film on AM60 magnesium alloy [J]. *Corrosion Science*, 2015, 100: 275–283.
- [14] ESMAILY M, SVENSSON J E, FAJARDO S, BIRBILIS N, JOHANSSON L G. Fundamentals and advances in magnesium alloy corrosion [J]. *Progress in Materials Science*, 2017, 89: 92–193.
- [15] CAO F Y, SONG G L, ATRENS A. Corrosion and passivation of magnesium alloys [J]. *Corrosion Science*, 2016, 111: 835–845.
- [16] HU Jun-hua, ZHANG Cai-li, CUI Bao-hong, BAI Kui-feng, GUAN Shao-kang, WANG Li-guo, ZHU Shi-jie. In vitro degradation of AZ31 magnesium alloy coated with nano  $TiO_2$  film by sol–gel method [J]. *Applied Surface Science*, 2011, 257: 8772–8777.
- [17] CAO Guo-qin, WANG Li-jie, FU Zhen-ya, HU Jun-hua, GUAN Shao-kang, ZHANG Cai-li, WANG Li-guo, ZHU Shi-jie. Chemically anchoring of  $TiO_2$  coating on OH-terminated  $Mg_3(PO_4)_2$  surface and its influence on the in vitro degradation resistance of Mg–Zn–Ca alloy [J]. *Applied Surface Science*, 2014, 308: 38–42.
- [18] MIRAK A R, DAVIDSON C J, TAYLOR J A. Study on the early surface films formed on Mg–Y molten alloy in different atmospheres [J]. *Journal of Magnesium and Alloys*,

- 2015, 3: 173–179.
- [19] KALB H, RZANY A, HENSEL B. Impact of microgalvanic corrosion on the degradation morphology of WE43 and pure magnesium under exposure to simulated body fluid [J]. *Corrosion Science*, 2012, 57: 122–130.
- [20] LELEU S, RIVES B, BOUR J, CAUSSE N, PÉBÈRE N. On the stability of the oxides film formed on a magnesium alloy containing rare-earth elements [J]. *Electrochimica Acta*, 2018, 290: 586–594.
- [21] SURESH S, GOWD G H, DEVAKUMAR M L S. Mechanical and wear characteristics of aluminium alloy 7075 reinforced with nano-aluminium oxide/magnesium particles by stir casting method [J]. *Materials Today: Proceedings*, 2020, 24: 273–283.
- [22] RAMKUMAR T, SELVAKUMAR M, CHANDRASEKAR P, MOHANRAJ M, KRISHNASHARMA R. Monitoring the neural network modelling of wear behaviour of Ti–6Al–4 V reinforced with nano B<sub>4</sub>C particle [J]. *Materials Today: Proceedings*, 2021, 41: 942–950.
- [23] WANG Z B, TAO N R, LI S, WANG W, LIU G, LU J, LU K. Effect of surface nanocrystallization on friction and wear properties in low carbon steel [J]. *Materials Science and Engineering A*, 2003, 352: 144–149.
- [24] CHEN Jun-xiu, DONG Jia-hui, FU Hua-meng, ZHANG Hai-feng, TAN Li-li, ZHAO De-wei, YANG Ke. In vitro and in vivo studies on the biodegradable behavior and bone response of Mg<sub>69</sub>Zn<sub>27</sub>Ca<sub>4</sub> metal glass for treatment of bone defect [J]. *Journal of Materials Science & Technology*, 2019, 35: 2254–2262.
- [25] DONG Kai-hui, SONG Ying-wei, SHAN Da-yong, HAN En-hou. Formation mechanism of a self-sealing pore micro-arc oxidation film on AM60 magnesium alloy [J]. *Surface & Coatings Technology*, 2015, 266: 188–196.
- [26] GU Y H, CHEN C F, BANDOPADHYAY S, NING C Y, ZHANG Y J, GUO Y J. Corrosion mechanism and model of pulsed DC microarc oxidation treated AZ31 alloy in simulated body fluid [J]. *Applied Surface Science*, 2012, 258: 6116–6126.
- [27] SHAHIN M, MUNIR K, WEN C E, LI Y C. Nano-tribological behavior of graphene nanoplatelet-reinforced magnesium matrix nanocomposites [J]. *Journal of Magnesium and Alloys*, 2021, 9: 895–909.
- [28] CHAN C W, QUINN J, HUSSAIN I, CARSON L, SMITH G C, LEE S. A promising laser nitriding method for the design of next generation orthopaedic implants: Cytotoxicity and antibacterial performance of titanium nitride (TiN) wear nano-particles, and enhanced wear properties of laser-nitrided Ti6Al4V surfaces [J]. *Surface & Coatings Technology*, 2021, 405: 126714.
- [29] WEI Bing-jian, CHENG Yu-lin, LIU Yuan-yuan, ZHU Zhun-da, CHENG Ying-liang. Corrosion and wear resistance of AZ31 Mg alloy treated by duplex process of magnetron sputtering and plasma electrolytic oxidation [J]. *Transactions of Nonferrous Metals Society of China*, 2021, 31: 2287–2306.
- [30] CHEN J X, LU S H, Tan L L, ETIM I P, YANG K. Comparative study on effects of different coatings on biodegradable and wear properties of Mg–2Zn–1Gd–0.5Zr alloy [J]. *Surface & Coatings Technology*, 2018, 352: 273–284.
- [31] XU He, LIU Jing-an, XIE Shui-sheng. Magnesium alloys fabrication and processing technology [M]. Beijing: China Metallurgical Industry Press, 2007. (in Chinese)
- [32] GAO J H, SHI X Y, YANG B, HOU S S, MENG E C, GUAN F X, GUAN S K. Fabrication and characterization of bioactive composite coatings on Mg–Zn–Ca alloy by MAO/sol–gel [J]. *Journal of Materials Science: Materials in Medicine*, 2011, 22: 1681–1687.
- [33] CHEN Shuai, S. GUAN Shao-kang, LI Wen, WANG Huan-xin, CHEN Juan, WANG Yi-sheng, WANG Hai-tao. In vivo degradation and bone response of a composite coating on Mg–Zn–Ca alloy prepared by microarc oxidation and electrochemical deposition [J]. *Journal of Biomedical Materials Research Part B: Applied Biomaterials*, 2012, 100: 533–543.
- [34] LU Ping, CAO LU, LIU Yin, XU Xin-hua, WU Xiang-feng. Evaluation of magnesium ions release, biocorrosion, and hemocompatibility of MAO/PLLA-modified magnesium alloy WE42 [J]. *Journal of Biomedical Materials Research Part B: Applied Biomaterials*, 2011, 96: 101–109.
- [35] WANG Xue-jian, CHEN Zong-ning, ZHANG Yu-bo, GUO En-yu, KANG Hui-jun, HAN Pei, WANG Tong-min. Influence of microstructural characteristics on corrosion behavior of Mg–5Sn–3In alloy in Hank’s solution [J]. *Transactions of Nonferrous Metals Society of China*, 2021, 31: 2999–3011.
- [36] WINDHAGEN H, RADTKE K, WEIZBAUER A, DIEKMANN J, NOLL Y, KREIMEYER U, SCHAVAN R, STUKENBORG-COLSMAN C, WAIZY H. Biodegradable magnesium-based screw clinically equivalent to titanium screw in hallux valgus surgery: short term results of the first prospective, randomized, controlled clinical pilot study [J]. *Biomedical Engineering Online*, 2013, 12: 62.
- [37] DIEKMANN J, BAUER S, WEIZBAUER A, WILLBOLD E, WINDHAGEN H, HELMECKE P, LUCAS A, REIFENRATH J, NOLTE I, EZECHIELI M. Examination of a biodegradable magnesium screw for the reconstruction of the anterior cruciate ligament: A pilot in vivo study in rabbits [J]. *Materials Science and Engineering C*, 2016, 59: 1100–1109.

# ZK60 合金表面含纳米 $Y_2O_3$ 微弧氧化涂层的体外降解、磨损性能和生物相容性

陈军修<sup>1,2</sup>, 杨洋<sup>1,2</sup>, Iniobong P. ETIM<sup>3</sup>, 谭丽丽<sup>3</sup>,  
杨柯<sup>3</sup>, R. D. K. MISRA<sup>4</sup>, 王建华<sup>1,2</sup>, 苏旭平<sup>1,2</sup>

1. 常州大学 江苏省材料表面科学与技术重点实验室, 常州 213164;

2. 常州大学 江苏省光伏科学与工程协同创新中心, 常州 213164;

3. 中国科学院 金属研究所, 沈阳 110016;

4. Department of Metallurgical, Materials and Biomedical Engineering, University of Texas, El Paso, TX, USA

**摘要:** 为了进一步降低镁合金微弧氧化(MAO)涂层的降解速率并提高其耐磨性能, 通过在电解液中加入纳米  $Y_2O_3$  的方法, 制备含纳米  $Y_2O_3$  的镁合金 MAO 涂层, 并借助显微结构观察、磨损实验、电化学实验、浸泡实验和细胞毒性实验对其进行研究。结果表明, 微弧氧化涂层中主要含有  $Ca_8YMg(PO_4)_7$  和  $Y_2O_3$  颗粒,  $Ca_8YMg(PO_4)_7$  能稳定涂层, 纳米  $Y_2O_3$  能封闭微孔, 从而降低涂层的降解速率, 并提高其耐磨性。在 Hank's 溶液中, 涂层的降解速率从 0.14 mm/a 降至 0.06 mm/a。在相同摩擦距离下, 涂层体积损失从 0.46 mm<sup>3</sup> 降至 0.27 mm<sup>3</sup>。MAO 涂层具有良好的生物相容性, 细胞相对增殖率(RGR)超过 90%。含纳米  $Y_2O_3$  的 MAO 涂层具有良好的生物医学应用前景。

**关键词:** 纳米  $Y_2O_3$ ; MAO 涂层; 磨损性能; 降解性能; 生物相容性

(Edited by Bing YANG)